

## Gas Kinematics and Cosmic-Ray Acceleration in the Gamma-ray SNRs W41 and G22.7–0.2

T. MURASE  <sup>1</sup> H. SANO  <sup>1,2,3</sup> K. MATSUBARA, <sup>1</sup> Y. FUKUI  <sup>1,4</sup> J. NISHI, <sup>5</sup> S. EINECKE  <sup>6</sup> M. D. FILIPOVIĆ  <sup>7</sup> R. KASAI  <sup>5</sup> R. MATSUSAKA  <sup>5,8</sup> G. ROWELL  <sup>6</sup> H. SODOH, <sup>9</sup> H. SUZUKI  <sup>10</sup> Y. SHIBATA  <sup>4,5</sup> K. TSUGE  <sup>1,11</sup> H. TAKABA, <sup>1,12</sup> AND T. HANNA  <sup>5,13,14</sup>

<sup>1</sup> Faculty of Engineering, Gifu University, 1-1 Yanagido, Gifu 501-1193, Japan

<sup>2</sup> Department of Intelligence Science and Engineering, Graduate School of Natural Science and Technology, Gifu University, 1-1 Yanagido, Gifu, 501-1193 Japan

<sup>3</sup> Center for Space Research and Utilization Promotion (c-SRUP), Gifu University, 1-1 Yanagido, Gifu 501-1193, Japan

<sup>4</sup> Department of Physics, Nagoya University, Furo-cho, Chikusa-ku, Nagoya 464-8601, Japan

<sup>5</sup> Department of Physics and Astronomy, Graduate School of Science and Engineering, Kagoshima University, 1-21-35 Korimoto, Kagoshima, Kagoshima 890-0065, Japan

<sup>6</sup> School of Physical Sciences, The University of Adelaide, North Terrace, Adelaide, SA 5005, Australia

<sup>7</sup> Western Sydney University, Locked Bag 1797, Penrith South DC, NSW 1797, Australia

<sup>8</sup> Institute of Astronomy, Graduate School of Science, The University of Tokyo, 2-21-1 Osawa, Mitaka, Tokyo 181-0015, Japan

<sup>9</sup> National Institute of Technology, Sendai College 48 Nodayama, Medeshima-Shiote, Natori, Miyagi 981-1239, Japan

<sup>10</sup> Faculty of Engineering, University of Miyazaki, Miyazaki 889-2192, Japan

<sup>11</sup> Institute for Advanced Study, Gifu University, 1-1 Yanagido, Gifu 501-1193, Japan

<sup>12</sup> National Astronomical Observatory of Japan, Mitaka, Tokyo 181-8588, Japan

<sup>13</sup> Amanogawa Galaxy Astronomy Research Center, Kagoshima University, 1-21-35 Korimoto, Kagoshima, Kagoshima 890-0065, Japan

<sup>14</sup> Division of Liberal Arts, Kogakuin University, 2665-1 Nakano-cho, Hachioji, Tokyo 192-0015, Japan

(Accepted January 24, 2026)

## ABSTRACT

We present a study of the interstellar medium associated with the two middle-aged supernova remnants (SNRs) W41 and G22.7–0.2, both detected in TeV gamma-rays. Using high-angular-resolution  $^{12}\text{CO}(J = 1-0)$  data from the Nobeyama 45-m telescope and HI data from the VLA, we investigated the spatial and kinematic properties of molecular and atomic gas that interact with the SNRs. We identified associated clouds in the velocity ranges of  $+50$ – $+80$  km s $^{-1}$  for W41 and  $+76$ – $+110$  km s $^{-1}$  for G22.7–0.2. Column density analysis indicates that target protons are dominated by molecular hydrogen, while atomic hydrogen contributes less than  $\sim 10$ – $15\%$  even after correction for self-absorption. The mean proton densities are  $\sim 1.2 \times 10^3$  cm $^{-3}$  for W41 and  $\sim 5.3 \times 10^2$  cm $^{-3}$  for G22.7–0.2. From the gamma-ray luminosities, we estimate the total energy of accelerated cosmic-ray protons as  $W_p$   $\sim 3 \times 10^{47}$  erg for W41 and  $\sim 1 \times 10^{48}$  erg for G22.7–0.2, corresponding to 0.03–0.1% of the canonical supernova explosion energy. These  $W_p$  values agree with the decreasing trend in  $W_p$  observed in the middle-aged SNRs within the previously reported SNR age– $W_p$  relation.

**Keywords:** Cosmic rays (329); Supernova remnants (1667); Interstellar medium (847); Gamma-ray sources (633)

## 1. INTRODUCTION

Since their discovery by Hess (1912), the origin of Galactic cosmic rays, which consist primarily of relativistic protons with energies up to  $\sim 3$  PeV, has remained one of the long-standing problems in modern astrophysics. Supernova remnants (SNRs) are considered the most plausible accelerators of such cosmic-rays, because their shocks, propagating at velocities of  $\sim 3,000$ – $10,000$  km s $^{-1}$ , provide an ideal environment for diffusive shock acceleration (DSA; e.g., Bell 1978;

Blandford & Ostriker 1978; Drury 1983). If SNRs are the dominant sources of Galactic cosmic rays, the total energy of accelerated cosmic-ray protons,  $W_p$ , per supernova explosion can be estimated from the Galactic cosmic-ray energy density, the confinement time in the disk, and the supernova rate, yielding a conventional value of  $10^{49}$ – $10^{50}$  erg (see a review by Gabici 2013). However, this estimate has not yet been observationally confirmed.

To observationally validate this value, it is essential to study the interstellar medium (ISM) associated with

hadronic gamma-ray SNRs. Cosmic-ray protons interact with ambient protons through p–p collisions to produce neutral pions, which subsequently decay into hadronic gamma rays. Thus, accurate determination of the total ISM proton content provides a direct means of deriving  $W_p$ . In many previous observational and theoretical studies, the ISM was approximated by ionized gas with a uniform density, typically assumed to be  $\sim 1 \text{ cm}^{-3}$  (e.g., Ellison et al. 2010; Lee et al. 2013; Yang et al. 2014). However, recent radio observations have demonstrated that such assumptions are not justified. High-resolution data have revealed highly inhomogeneous ISM structures, including optically thick HI, coincident with SNR shells, and have confirmed that the dominant target material consists of neutral molecular and atomic hydrogen (e.g., Fukui et al. 2003, 2012, 2015, 2017; Yoshiike et al. 2013; Aruga et al. 2022; Sano et al. 2017, 2018, 2021a,b, 2022).

Even when the target gas density is derived by considering both molecular and atomic components and the  $W_p$  is estimated from the comparison with the observed gamma-ray luminosity, the physical interpretation of  $W_p$  requires careful attention. This is because gamma-ray emission from SNRs reflects the time evolution of cosmic-ray acceleration, diffusion, and escape. Recent studies have shown that cosmic-ray acceleration nearly terminates within a few hundred to a thousand years after the explosion, during the free-expansion phase, at which time  $W_p$  is determined (e.g., Tsuji et al. 2021; Suzuki et al. 2021). Sano et al. (2021a,b, 2022) analyzed 13 gamma-ray emitting SNRs older than  $\sim 1$  kyr where CR acceleration is nearly complete—and derived the relation between the SNR age and  $W_p$ . They found a positive correlation for SNRs aged 1–6 kyr and a negative correlation for those older than 8 kyr, which they interpreted as a consequence of cosmic-ray diffusion and escape. The increasing trend in young SNRs can be explained in the framework of age-limited acceleration (e.g., Ohira et al. 2010; Telezhinsky et al. 2012), where the finite age of the remnant constrains the maximum acceleration time. An alternative explanation is that the degree of cosmic-ray penetration into the stellar-wind shell evolves over time, resulting in a time-dependent gamma ray luminosity (see also Sano et al. 2023). In contrast, the decreasing trend observed in middle-aged SNRs is generally attributed to energy-dependent diffusion (e.g., Aharonian & Atoyan 1996; Gabici 2013). In this process, high-energy cosmic rays gradually escape from the SNR shell and diffuse into the surrounding ISM, leading to a decrease in the inferred total proton energy  $W_p$  with increasing SNR age. Such behavior has also been discussed for W44 (e.g., Uchiyama et al. 2012).

However, the number of middle-aged SNRs with well-constrained  $W_p$  values remains limited. The next key step is to increase the statistical sample of such remnants and to observationally verify the unified picture

of cosmic ray acceleration and diffusion throughout SNR evolution.

W41 and G22.7–0.2 are both middle-aged SNRs with detected gamma-ray emission, making them ideal laboratories for investigating the age– $W_p$  relation. Their ages are estimated to be  $\sim 60$  kyr and  $\sim 20$  kyr, respectively (e.g., Stafford et al. 2019; Suzuki et al. 2021). H.E.S.S. observations have identified HESS J1834–087 and HESS J1832–093 as their gamma-ray counterparts (H. E. S. S. Collaboration et al. 2015, 2018). Castro et al. (2013) performed broadband spectral modeling of Fermi-LAT and H.E.S.S. data for W41 and concluded that the gamma-ray emission is of hadronic origin. They argued that the leptonic scenario is disfavored, since reproducing the observed spectrum would require an electron-to-proton ratio as high as  $\sim 10\%$ . For G22.7–0.2, comparisons with Galactic ridge spectra suggest that its gamma-ray emission most likely originates from proton interactions with nearby molecular clouds, although its origin remains uncertain (H. E. S. S. Collaboration et al. 2015; Tam et al. 2020). Interstellar molecular and atomic clouds associated with these SNRs have also been discussed in previous studies (e.g., Leahy & Tian 2008; Frail et al. 2013; Su et al. 2014, 2015). Notably, Frail et al. (2013) detected shock-excited 1720 MHz OH masers with a line-of-sight velocity of  $\sim +74 \text{ km s}^{-1}$  toward the central radio shell of W41, providing strong evidence for interaction between the SNR shock and molecular clouds. However, the limited angular resolution of previous CO data ( $\sim 46''$ ) has precluded detailed spatial and kinematic analyses of the associated gas, and the identification and quantitative characterization of the target ISM interacting with cosmic rays remain incomplete.

In this study, we aim to identify and analyze the associated ISM around W41 and G22.7–0.2 using high angular resolution CO and HI data obtained with the Nobeyama 45-m Telescope and the VLA. The Nobeyama CO data provide an unprecedented angular resolution of  $\sim 20''$ , enabling precise identification of molecular clouds interacting with the SNRs. The structure of this paper is as follows. Section 2 describes the observational data and analysis methods. Section 3 is divided into three subsections: Section 3.1 presents the distributions of radio continuum and gamma rays; Section 3.2 describes the spatial and velocity structures of the CO and HI gas; and Section 3.3 discusses the HI brightness dips at the locations of CO emission. The discussion and conclusions are given in Sections 4 and 5.

## 2. DATA SETS

### 2.1. Radio continuum

To investigate the spatial distribution of the SNR shells, we used the 20 cm radio continuum data taken from the Multi-Array Galactic Plane Imaging Survey (MAGPI; Helfand et al. 2006). The spatial resolution

is  $6''.4 \times 5''.4$  with a position angle of  $350^\circ$ . The typical rms noise is  $\sim 0.3$  mJy beam $^{-1}$ .

## 2.2. $HI$

We used the HI line data from the VLA Galactic Plane Survey (VGPS; Stil et al. 2006). The spatial resolution of HI cube data was  $60''$ . The typical rms noise level is  $\sim 2$  K at a velocity channel width of  $0.824$  km s $^{-1}$ . Details on observing techniques and data processing are given in Stil et al. (2006).

## 2.3. H.E.S.S. $TeV$ Gamma Rays

We used archival gamma-ray Galactic Plane survey data obtained by the High Energy Stereoscopic System (H.E.S.S.; H. E. S. S. Collaboration et al. 2018). In this study, we used the gamma-ray significance maps generated with a standard correlation radius  $R_c = 0''.1$ . The 68% containment radii of point-spread function (PSF) is  $0''.08$ . For more details, see H. E. S. S. Collaboration et al. (2018).

## 2.4. $CO$

### 2.4.1. Observations

$^{12}\text{CO}(J = 1-0)$  line data were obtained as part of the FOREST Unbiased Galactic plane Imaging Survey with the Nobeyama 45-m telescope (FUGIN; Umemoto et al. 2017). These data were obtained using the multi-beam receiver, FOOr-beam REceiver System on the 45-m Telescope (FOREST; Minamidani et al. 2016). The observations were made by the On-The-Fly (OTF) mapping mode (Sawada et al. 2008). The half-power beam width (HPBW) is  $\sim 14''.4$  at 115 GHz. The overall map is made by connecting  $1^\circ \times 1^\circ$  mosaic sub-maps. The spectrometer was the Spectral Analysis Machine for the 45-m (SAM45; Kuno et al. 2011) with 4,096 channels, providing a velocity resolution of  $1.3$  km s $^{-1}$  at 115 GHz. See Umemoto et al. (2017) for a detailed observing strategy and OTF scan parameters.

### 2.4.2. Data reduction

Since published FUGIN data are contaminated with stripe structures along the scan direction, we performed self-reduction in  $^{12}\text{CO}(J = 1-0)$  line for the range of  $21^\circ 0 < l < 25^\circ 0$ ,  $|b| < 1^\circ 0$ . Data reduction was performed using NOSTAR software provided by the Nobeyama Radio Observatory (see Section 5.1 in Sawada et al. 2008). For each  $1^\circ \times 1^\circ$  mosaic sub-map, the following data processing was performed:

1. Split raw data files into individual arrays.
2. The intensity variation of each array was calibrated with daily mapping observations towards W51D [ $\alpha_{\text{B1950}} = 19^\text{h}21^\text{m}22^\text{s}.2$ ,  $\delta_{\text{B1950}} = 14^\circ25'17''.0$ ].

3. Baseline subtraction was performed with a third-order polynomial function. The baseline ranges are from  $-250$  to  $-100$  and from  $+200$  to  $+350$  km s $^{-1}$ .

Maps are produced as a cube FITS by gridding over the desired area. The Gridding Convolution Function (GCF) was used the Bessel  $\times$  Gaussian function. Finally, we made a cube FITS with a spatial grid interval of  $8''.5$  and velocity interval of  $0.65$  km s $^{-1}$ . The effective angular resolution was  $20''.2$  for  $^{12}\text{CO}(J = 1-0)$ . Additionally, a baseline subtraction was performed using a third-order polynomial function on the FITS of the produced cube. The baseline ranges were determined manually for each on-source scan.

The produced maps suffer from scanning noise (also known as *scanning effect*) in addition to thermal noise. Scanning effects are usually subtracted by the basket-weave method, which combines two maps produced from orthogonal scans (e.g., Emerson & Graeve 1988; Müller et al. 2017). However, in the  $21^\circ 0 < l < 25^\circ 0$  region, only the scan parallel to the Galactic plane (X-scan) was observed due to instrumental trouble. In this study, we used the PRESS method (Sofue & Reich 1979; Sofue 2019) for the subtraction of the scanning effects.

## 3. RESULTS

### 3.1. Overview of Gamma-rays and Radio Continuum

Figure 1 shows the radio continuum and H.E.S.S. gamma-ray significance maps of W41 and G22.7–0.2. Both SNRs exhibit radio shells with an angular diameter of  $\sim 30'$  and are located adjacent to each other around  $(l, b) = (23^\circ 0, -0^\circ 3)$ . However, their morphologies and correspondence with the gamma-ray emission differ.

W41 shows a well-defined shell, with particularly bright emission at its center  $(l, b) = (23^\circ 3, -0^\circ 3)$  and along the southern rim  $(l, b) = (23^\circ 0, -0^\circ 3)$ . In contrast, G22.7–0.2 has a relatively faint shell with a concave feature on its western side at  $(l, b) = (22^\circ 8, -0^\circ 1)$ . In gamma-rays, HESS J1834–087, related to W41, extends around the center of the shell with a peak significance of  $\sim 17\sigma$ . HESS J1832–093, related to G22.7–0.2, appears as a clumpy feature on southwest side of the shell at  $(l, b) = (22^\circ 5, -0^\circ 2)$ , with a peak significance of  $\sim 6\sigma$ .

Additionally, radio continuum brightest peaks on the two SNRs,  $(l, b) = (22^\circ 7, -0^\circ 5)$  and  $(23^\circ 4, -0^\circ 2)$ . However, as Figure 1 (b) shows, these do not coincide with the gamma-ray peaks. The former corresponds to the massive star-forming region G23.43–0.18 (e.g., Leahy & Tian 2008; Brunthaler et al. 2009; Fujisawa et al. 2014; Chibueze et al. 2025), for which the distance has been estimated as  $5.88^{+1.37}_{-0.93}$  kpc based on annual parallax measurements of methanol masers (Brunthaler et al. 2009). On the other hand, the kinematic distance of the molecular clouds related to W41 and G22.7–0.2 is  $\sim 4.4$  kpc (Frail et al. 2013; Su et al. 2014, 2015), suggesting a lack of physical association. The latter peak has been iden-

tified as either an SNR candidate (Helfand et al. 2006) or as an HII region (Thompson et al. 2006). Its spectral index has been measured as  $-0.98$  (Messineo et al. 2010). In either case, these radio continuum sources are unrelated to the present study and are excluded from further discussion.

### 3.2. Distribution of Radio continuum, CO and HI

Figures 2 and 3 present the  $^{12}\text{CO}(J = 1-0)$  and HI channel maps toward W41 and G22.7–0.2, respectively. In this paper, we focus on the velocity range from  $+45$  to  $+120 \text{ km s}^{-1}$ , which includes the line-of-sight velocity of the shock-excited 1720 MHz OH maser. The HI channel maps presented in Figures 2 and 3 use a limited color scale optimized to emphasize the large-scale spatial correspondence with the radio continuum shell. It should be noted that they do not display the full dynamic range, including the absorption features.

For W41, CO emission in the  $+55$ – $+60 \text{ km s}^{-1}$  range surrounds the radio shell from the southern to western sides and continues to the northern boundary. A diffuse, weak component with a brightness temperature of  $\sim 5 \text{ K}$  is also present at the shell center. At  $+70$ – $+80 \text{ km s}^{-1}$ , molecular gas associated with GMC G23.3–0.4 extends across the shell, showing a bright CO peak of  $\sim 11 \text{ K}$  at  $(l, b) = (23^\circ 3, -0^\circ 3)$ . This CO emission corresponds well with a weak HI feature ( $\sim 60 \text{ K}$  in brightness temperature) seen in the same velocity range. In HI maps, weak clouds with brightness temperatures of  $30$ – $60 \text{ K}$  spatially coincide with the radio shell at  $\sim +60 \text{ km s}^{-1}$ . Such correspondence is widely found over the  $+50$ – $+80 \text{ km s}^{-1}$  range. In addition, the northern side of the shell at  $(l, b) = (23^\circ 4, -0^\circ 2)$  shows an HI depression across nearly the entire velocity range (see Figure 5, position A, for the detailed HI line profile). Clumpy CO features are also seen in this region, corresponding to the massive star-forming region G23.43–0.18 (e.g., Leahy & Tian 2008; Brunthaler et al. 2009; Fujisawa et al. 2014; Chibueze et al. 2025).

For G22.7–0.2, CO emission spreads diffusely within the radio shell over  $+50$ – $+115 \text{ km s}^{-1}$ . Notably, at  $+75$ – $+80 \text{ km s}^{-1}$ , a CO cloud at the eastern edge  $(l, b) = (22^\circ 8, -0^\circ 4)$  shows well spatial agreement with the radio shell. A CO clump with  $\sim 12 \text{ K}$  brightness temperature is also identified in the southern shell at  $(l, b) = (22^\circ 6, -0^\circ 1)$ . In comparison with HI, no clear correlation is seen in the  $+45$ – $+70 \text{ km s}^{-1}$  range. However, at  $+70$ – $+95 \text{ km s}^{-1}$  and  $+105$ – $+110 \text{ km s}^{-1}$ , weak HI clouds with brightness temperatures of  $\sim 60 \text{ K}$  align well with the shell. Furthermore, local depressions of  $\sim 30 \text{ K}$  are observed at  $(l, b) = (22^\circ 6, -0^\circ 1)$  in  $+70$ – $+75 \text{ km s}^{-1}$ , at  $(l, b) = (22^\circ 6, -0^\circ 2)$  in  $+75$ – $+80 \text{ km s}^{-1}$ , and at  $(l, b) = (22^\circ 8, -0^\circ 3)$  in  $+105$ – $+110 \text{ km s}^{-1}$ . These depressions spatially coincide with CO emission.

Figure 4 shows the longitude–velocity maps of CO and HI. Two cavity-like structures are identified in the CO map: one at  $23^\circ 1 < l < 23^\circ 5$  and  $+50$ – $+80 \text{ km s}^{-1}$ , and

another at  $22^\circ 5 < l < 23^\circ 0$  and  $+75$ – $+110 \text{ km s}^{-1}$ . The longitudinal extents of these structures are nearly correspond to the diameters of their respective SNR shells. In the corresponding regions, the HI maps also exhibit faint emission ( $\sim 12 \text{ K deg}$ ). Figure 4(b) shows that low-brightness HI features of  $\sim 10$ – $13 \text{ K deg}$  are observed at  $(l, v) = (22^\circ 6, +80 \text{ km s}^{-1})$ ,  $(22^\circ 7, +110 \text{ km s}^{-1})$ ,  $(23^\circ 4, +80 \text{ km s}^{-1})$ , and  $(23^\circ 4, +100 \text{ km s}^{-1})$ , which is in good agreement with the CO distribution. Conversely, at  $(l, v) = (23^\circ 1, +60 \text{ km s}^{-1})$ , faint HI ( $\sim 10 \text{ K deg}$ ) is detected without corresponding CO emission. Additionally, aligned low-brightness HI features are seen over  $+40$ – $+110 \text{ km s}^{-1}$  around  $l = 23^\circ 4$ , with pronounced depressions at  $+80$  and  $+100 \text{ km s}^{-1}$ , which again coincide with CO. In contrast, no corresponding CO emission is detected in the  $+40$ – $+70 \text{ km s}^{-1}$  range. This series of faint HI features corresponds to the massive star-forming region G23.43–0.18, which is located at  $v_{\text{LSR}} \sim +100 \text{ km s}^{-1}$ .

### 3.3. Analysis of the CO and HI spectral

To distinguish whether the low-brightness HI coincident with the radio continuum are due to absorption by the background continuum or self-absorption caused by cold HI embedded in molecular gas, we compared the HI and CO spectra. For both W41 and G22.7–0.2, we selected regions in which the low HI brightness temperature corresponds to the radio shell. Then, we constructed line profiles at each position. Figure 5 shows the integrated intensity maps of CO and HI, together with representative line profiles at selected positions. Of the positions shown in Figures 5(a)–(d), positions A–C correspond to W41 and positions D–F correspond to G22.7–0.2.

At positions A–C, the HI emission generally peaks near  $+70 \text{ km s}^{-1}$  and  $+85 \text{ km s}^{-1}$ . Position A lies in a region containing a massive star-forming region in the background, where deep HI dips reaching the lowest brightness ( $\sim 90 \text{ K}$ ) are observed between  $+80$  and  $+100 \text{ km s}^{-1}$ . These features are consistent with absorption against strong background continuum emission (brightness temperature  $\sim 180 \text{ K}$ ; Stil et al. 2006). However, CO emission coincident with the HI dips is also detected at both velocities. This suggests that both absorption against the continuum background and self-absorption by cold HI clouds located in front of it may both contribute. In contrast, at positions B and C, prominent HI dips with depths of  $30$ – $50 \text{ K}$  and line widths of a few  $\text{km s}^{-1}$  are observed near  $+60 \text{ km s}^{-1}$  and  $+78 \text{ km s}^{-1}$ , showing well spatial and velocity correspondence with  $^{12}\text{CO}$  emission.

For positions D–F, the features are less prominent. However, HI peaks are seen around  $+90 \text{ km s}^{-1}$  and  $+110 \text{ km s}^{-1}$ , showing slight saturation. Additionally, HI dips with depths of  $20$ – $50 \text{ K}$  are found near  $+75 \text{ km s}^{-1}$  and  $+100 \text{ km s}^{-1}$  at all positions, again showing good correspondence with CO emission.

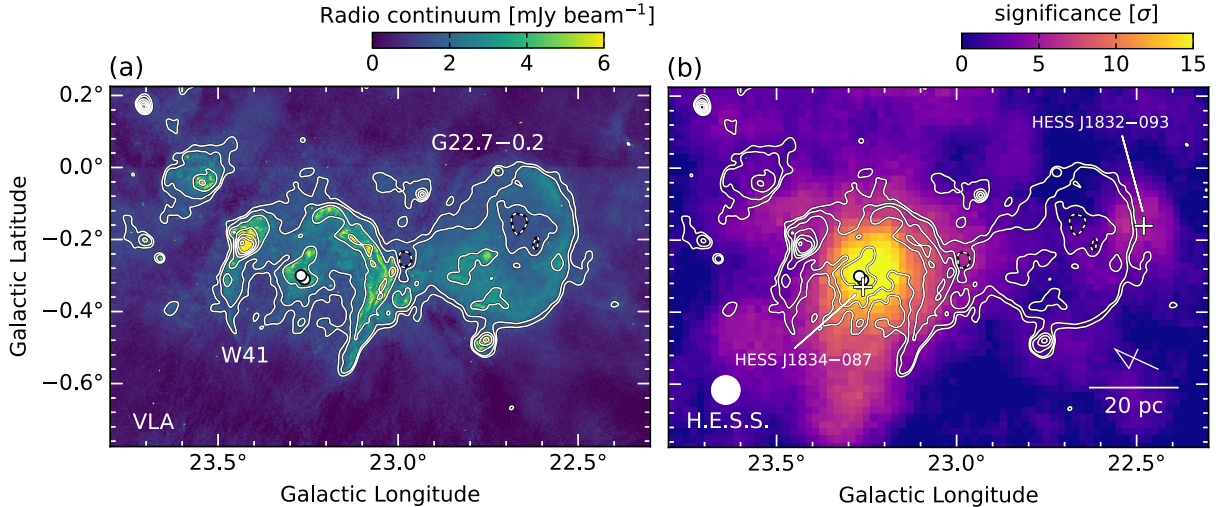


**Figure 1.** Maps of (a) 20 cm radio continuum from the MAGPIS survey (Helfand et al. 2006), (b) TeV gamma-ray significance map obtained from H.E.S.S. (H. E. S. Collaboration et al. 2018) toward the SNRs W41 and G22.7–0.2. The superposed contours are 20 cm radio continuum. The contour levels are 1.40, 1.75, 2.80, 4.55, 7.00, 10.15, and 14.00 mJy beam<sup>−1</sup>. The circles indicate the positions of the 1720 MHz OH maser (Frail et al. 2013). The positions of TeV gamma-ray sources are indicated by the white crosses in Figure 1(b).

To interpret these behaviors, we briefly summarize the HI–H<sub>2</sub> transition. It is well recognized that atomic hydrogen is converted into molecular hydrogen on dust grain surfaces as the column density and ultraviolet shielding increase (e.g., Allen & Robinson 1977). Accordingly, the distributions of cold HI and CO emission are generally similar, as both trace the dense, shielded regions within molecular clouds. Based on these results, we conclude that the HI absorption dips observed at positions B–F are predominantly due to self-absorption by cold HI within the CO-emitting molecular clouds.

#### 4. DISCUSSION

##### 4.1. Molecular clouds associated with the SNR W41 and G22.7–0.2

Previous ISM studies of W41 and G22.7–0.2 have suggested the presence of associated molecular clouds, based on the detection of a shock-excited 1720 MHz OH maser at  $\sim +74$  km s<sup>−1</sup> and molecular clouds crossing both SNRs (e.g., Lee et al. 2013; Frail et al. 2013; Su et al. 2014, 2015; Hogge et al. 2019). However, comprehensive analyses using both CO and HI data are lacking, and interacting clouds have not been firmly identified. In this section, we argue that the molecular and atomic clouds physically associated with W41 and G22.7–0.2 are found in the velocity ranges of  $+50$ – $+80$  km s<sup>−1</sup> and  $+76$ – $+110$  km s<sup>−1</sup>, respectively. Identifying the SNR-associated clouds requires not only investigating spatial distributions but also considering velocity structures and HI absorption features. We then evaluate the consistency of these results with previously reported gas components. Specifically, Section 4.1.1 describes the spatial distribution of the clouds and HI absorption,

Section 4.1.2 addresses their velocity structures, and Section 4.1.3 discusses consistency with previous studies.

##### 4.1.1. Spatial Distributions and HI absorption

First, we show the spatial correspondence between the radio continuum shells and the molecular gas (Figures 2, 3, and Section 3.2). In W41, CO emission in the  $+55$ – $+60$  km s<sup>−1</sup> range is distributed so as to wrap around the southern to western to northern boundaries of the shell. In addition, at  $+70$ – $+80$  km s<sup>−1</sup>, a bright CO feature with  $T_{\text{mb}} \sim 11$  K is found at the shell center ( $l, b$ ) = (23.3,  $-0.3$ ), coinciding in both position and velocity with the shock-excited 1720 MHz OH maser. These features strongly suggest interactions between the SNR shock and molecular clouds. In G22.7–0.2, CO emission includes diffuse components extending across the shell interior as well as concentrations along its periphery. Notably, at  $+75$ – $+80$  km s<sup>−1</sup>, a CO cloud near ( $l, b$ ) = (22.8,  $-0.4$ ) shows excellent spatial agreement with the radio shell, forming a typical structure indicative of shock-cloud interaction. This correspondence implies that magnetic field amplification at the shocked cloud surface enhances synchrotron emission (e.g., Inoue et al. 2009, 2012; Sano et al. 2013).

The HI distribution also shows noteworthy spatial correlations. In W41, weak HI is detected at  $+55$ – $+60$  km s<sup>−1</sup> closely trace the radio shell, and in several regions, weak HI coincides with CO features. In G22.7–0.2, weak HI is found both inside the shell and along its southern rim, overlapping spatially with CO. These intensity depressions are not caused by absorption against the radio continuum background, but rather by

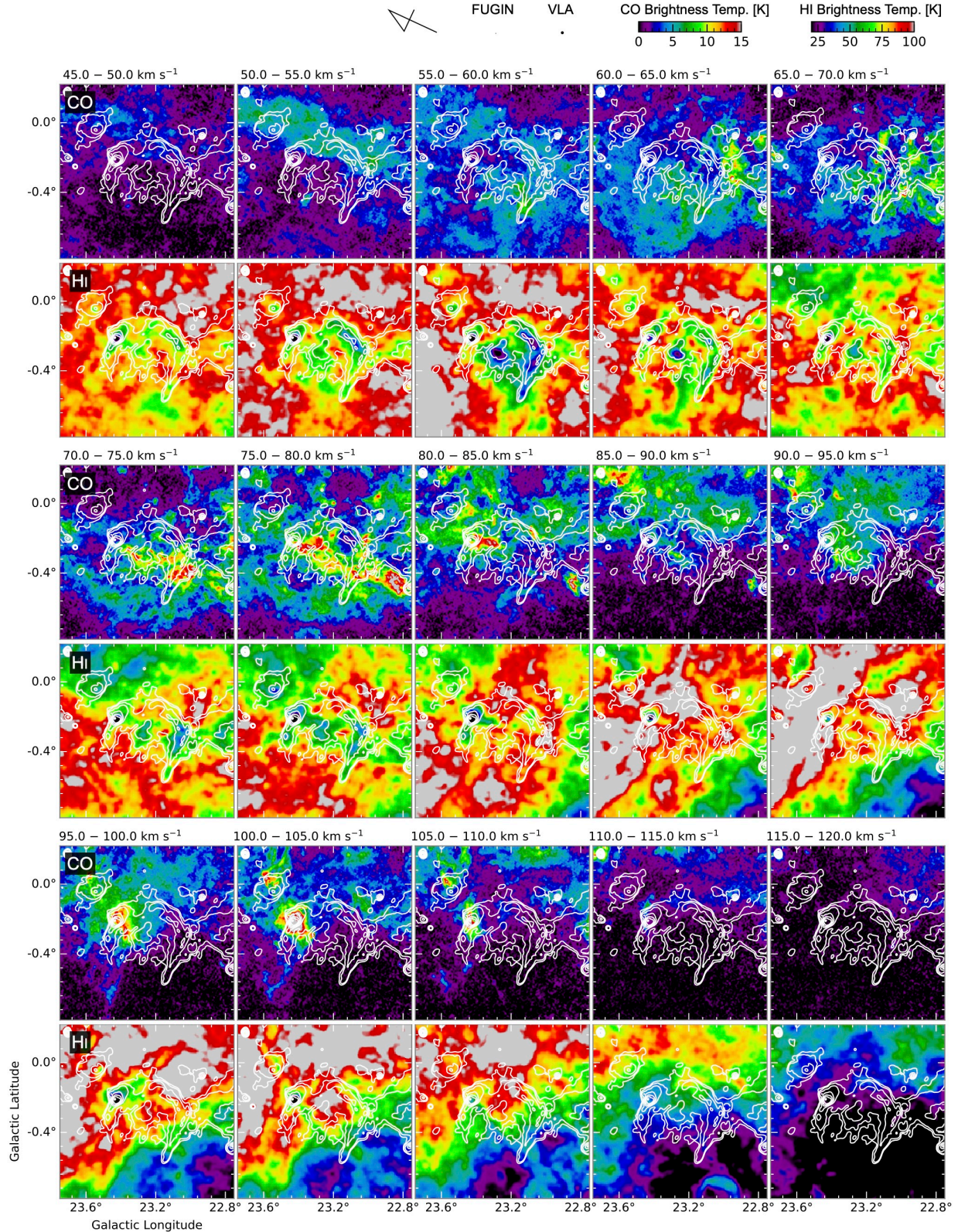


**Figure 2.** Velocity channel distributions of the  $^{12}\text{CO}(J = 1-0)$  and HI brightness temperatures towards W41 superposed with the same radio continuum contours as in Figure 1(a). Each panel shows intensity distributions averaged every  $5 \text{ km s}^{-1}$  in a velocity range from  $+45$  to  $+120 \text{ km s}^{-1}$ . The color bar is shown on top of the set of panels.

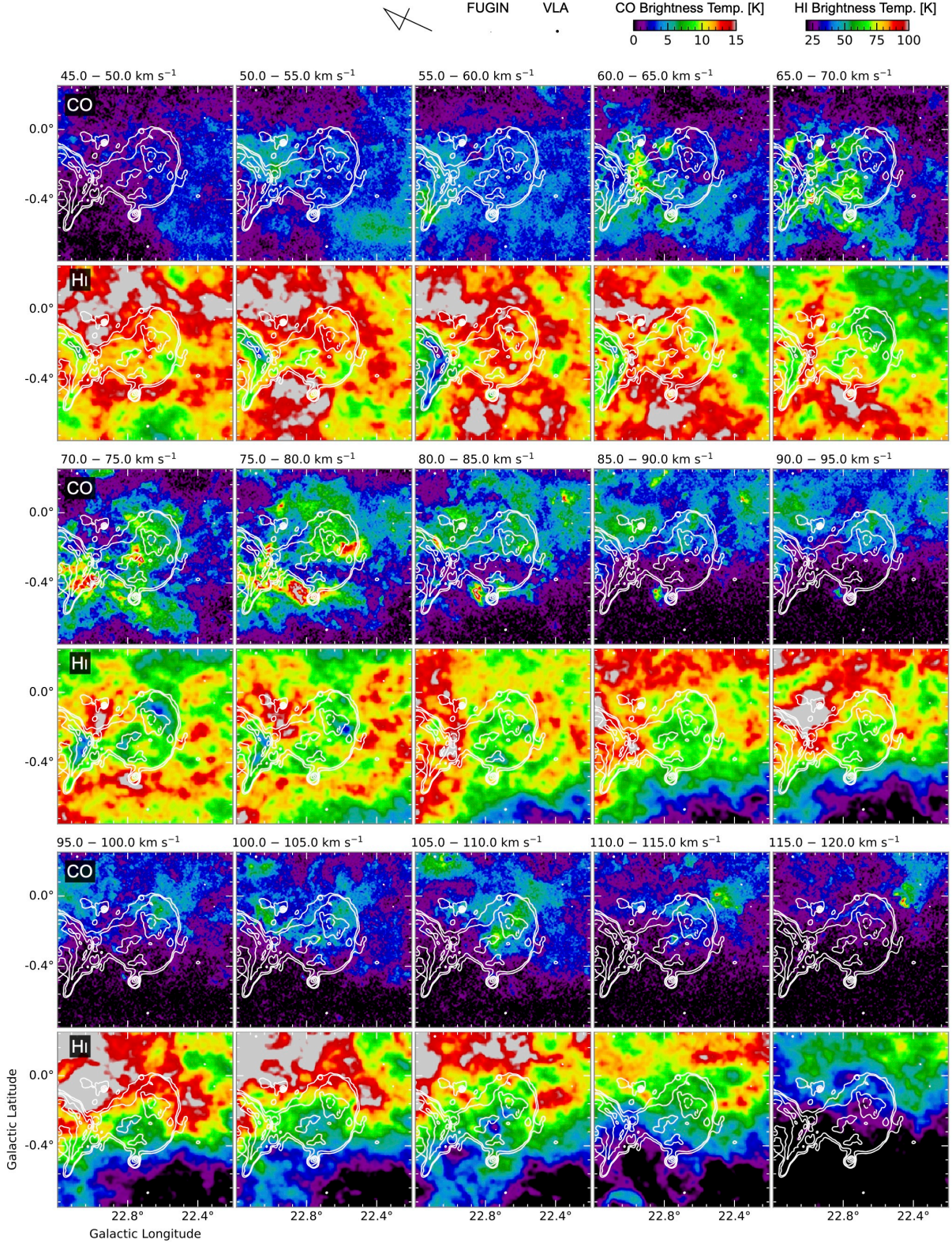


**Figure 3.** Same velocity channel maps as shown in Figure 2, but it is centered on G22.7-0.2.

self-absorption from cold HI embedded within molecular clouds (see Section 3.3). Thus, the observed HI characteristics indicate that the atomic and molecular

gas locate the same three-dimensional regions, supporting the conclusion that both are physically associated with the SNRs.

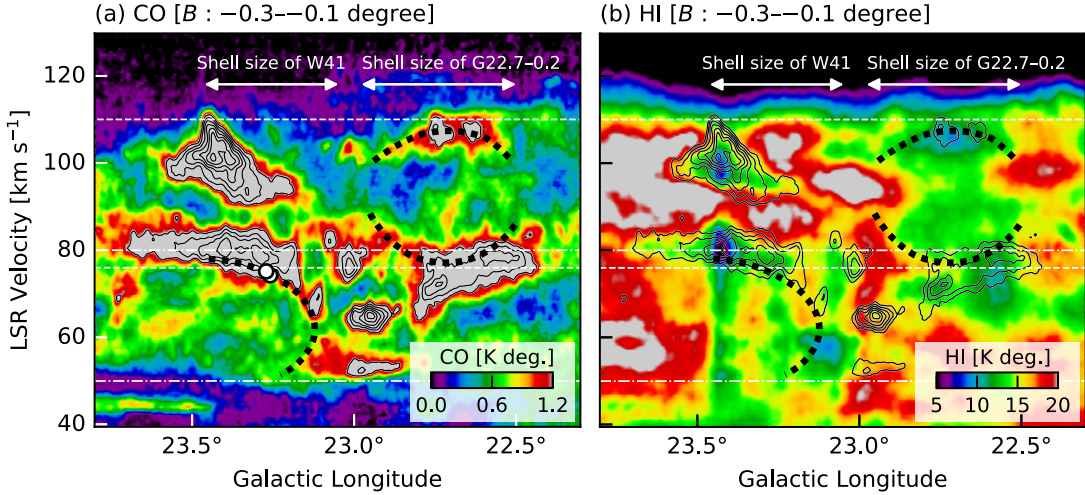


**Figure 4.** Longitude–Velocity diagrams of (a)  $^{12}\text{CO}(J = 1-0)$  and (b) HI. The integrated range is from  $-0^{\circ}3$  to  $-0^{\circ}1$  in the Galactic Latitude. The double-headed arrows indicate the diameter of each SNR shell. The dashed black curves show the expanding gas motion for each SNR (see the text). Horizontal dashed and one-dot chain lines indicate the integration velocity ranges for each SNR. The superposed contours in each panel indicate  $^{12}\text{CO}(J = 1-0)$ , whose contour levels are 1.2, 1.5, 1.8, 2.1, 2.4, 2.7, 3.0, and 3.3, K deg. The white filled circles represent the positions of the 1720 MHz OH masers (Frail et al. 2013).

#### 4.1.2. Expanding Gas Motion

Figure 4 shows cavity-like velocity structures in the  $l$ – $v$  diagrams, which provide compelling evidence of interactions between the SNR shocks and the surrounding medium. Such cavity features show expanding gas motions and are typically interpreted as wind-blown bubbles formed by stellar winds. These structures are thought to result from the combined action of strong winds from the progenitor star and the subsequent supernova shock wave (e.g., Koo et al. 1990; Koo & Heiles 1991; Koo & McKee 1992; Dwarkadas 2005).

We found cavity-like structures extending over  $+50$  to  $+80$   $\text{km s}^{-1}$  toward W41 and  $+75$  to  $+110$   $\text{km s}^{-1}$  toward G22.7–0.2 (Figure 4). From the  $l$ – $v$  diagrams, we defined the systemic velocity as the velocity where the cavity shows its maximum spatial extent and derived the expansion velocities accordingly. For W41, the systemic velocity is approximately  $+63$   $\text{km s}^{-1}$  with an expansion velocity of  $\sim 17$   $\text{km s}^{-1}$ ; for G22.7–0.2, the corresponding values are  $+92.5$   $\text{km s}^{-1}$  and  $\sim 17.5$   $\text{km s}^{-1}$ . Although these expanding velocities are smaller than typical SN shock velocities, the apparent bubble sizes are roughly consistent with the observed radio continuum shells (Figure 4). This suggests that the SN shocks propagate rapidly through the bubble interiors because the gas density and its gradient are extremely low, reducing deceleration (e.g., Weaver et al. 1977; Dwarkadas 2005; Broersen et al. 2014). Therefore, the detected bubbles are likely to have been formed by the strong stellar winds from the progenitor and are now interacting with supernova shock waves.

This scenario is further supported by the clear spatial correspondence between the shock-excited 1720 MHz

OH maser and the CO clouds in W41. The OH maser has a velocity of  $\sim +74$   $\text{km s}^{-1}$  and is located near the center of the radio shell (see Figure 1(a)). In velocity space, the maser lies on the boundary of the CO cloud, within the extent of the bubble (see Figure 4(a)). Although the projection geometry differs, such associations between molecular clouds and OH masers have also been reported in other Galactic SNRs (e.g., Arikawa et al. 1999; Sano et al. 2021a), providing a representative example of SNR shocks interacting with molecular clouds.

The expansion velocities identified in this study are larger than the values of several Galactic and Magellanic SNRs (e.g., a few  $\text{km s}^{-1}$  to  $\sim 10$   $\text{km s}^{-1}$ ; Landecker et al. 1989; Fukui et al. 2012; Sano et al. 2017, 2018, 2019, 2022; Kuriki et al. 2018; Fukushima et al. 2020; Aruga et al. 2022; Yeung et al. 2023; Ito et al. 2025). This suggests that the observed motions may not only reflect the intrinsic evolution of the SNRs but also be influenced by their surrounding environment. The GMC G23.3–0.4, to which both W41 and G22.7–0.2 belong, hosts multiple SNRs, young massive stars, and red supergiants. Spectroscopic studies have reported that massive star formation has been ongoing in this region over several tens of Myr (Messineo et al. 2014). It is therefore probable that the progenitor winds of the currently observed SNRs began expanding within low-density environments created by previous generations. This possibility is further supported by the nearly circular and symmetric shapes of the radio shells of both SNRs (Figure 1(a)), which are consistent with their expansion into a relatively homogeneous and low-density medium. Nevertheless, a detailed investigation of this issue lies beyond the scope of the present study. To better

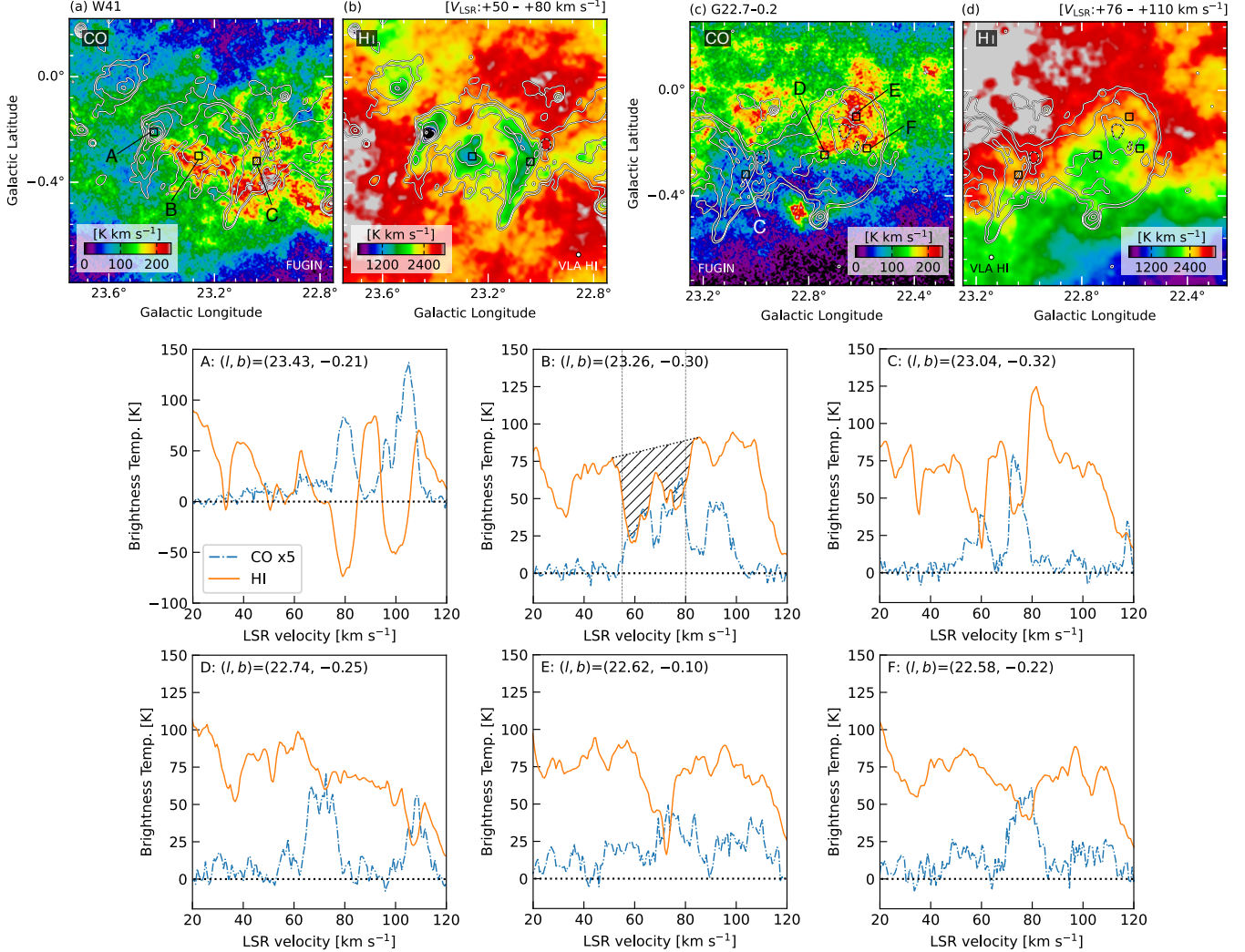


**Figure 5.** Integrated intensity maps of the  $^{12}\text{CO}(J = 1-0)$  and HI emission toward (a), (b) W41 in the velocity range  $v_{\text{LSR}} = +50-+80 \text{ km s}^{-1}$ , and (c), (d) G22.7–0.2 in the range  $v_{\text{LSR}} = +76-+110 \text{ km s}^{-1}$ . Black boxes mark the positions where line profiles were extracted. Line profiles shown below indicate  $^{12}\text{CO}(J = 1-0)$  (Blue) and HI (orange) at six positions: A ( $(l, b) = (23^\circ 43, -0^\circ 21)$ ), B ( $(23^\circ 26, -0^\circ 30)$ ), C ( $(23^\circ 04, -0^\circ 32)$ ), D ( $(22^\circ 74, -0^\circ 25)$ ), E ( $(22^\circ 62, -0^\circ 10)$ ), and F ( $(22^\circ 58, -0^\circ 22)$ ). The shaded area and vertical dashed lines in Position B indicates an expected background HI profile and a velocity range from +55 to +80  $\text{km s}^{-1}$ .

understand the connection between the surrounding environment and the subsequent evolution of SNRs, future observational and theoretical studies will be required.

#### 4.1.3. Consistency and Comparison with Previous Studies

Based on the above results, we conclude that the molecular and atomic clouds physically associated with W41 and G22.7–0.2 correspond to the velocity ranges of  $+50-+80 \text{ km s}^{-1}$  and  $+76-+110 \text{ km s}^{-1}$ , respectively. This conclusion is supported by their spatial distributions, velocity structures, and the presence of OH masers. The wind-blown bubbles identified in both SNRs overlap in the  $+76-+80 \text{ km s}^{-1}$  range, suggesting a possible physical interaction with GMC G23.3–0.4,

which is observed in the  $+70-+80 \text{ km s}^{-1}$  velocity range. This interpretation is consistent with previous CO and HI studies (e.g., Albert et al. 2006; Leahy & Tian 2008; Frail et al. 2013; Su et al. 2014, 2015).

Our analysis reveals that the two SNRs exhibit different systemic velocities. These results provide clues to the three-dimensional spatial relation between the SNRs and their associated molecular clouds. The GMC G23.3–0.4 shows a continuous spatial distribution extending from the central region of the W41 radio shell to the eastern rim of the G22.7–0.2 shell (Figure 5(a)), making it natural to regard them as part of the same molecular cloud. As shown in Figure 4(a), the interacting components of the SNRs relative to the GMC indicating

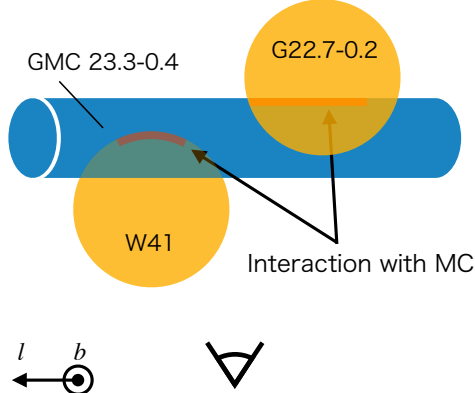


**Figure 6.** Schematic top-down view of the relative positions of the two SNRs and the GMC. The orange ellipses represent the SNR bubbles and the blue cylinder shows the GMC G23.3-0.4. The thick red lines highlight the regions where the SNRs interact with the GMC. The shell of W41 is located in front of the GMC, while G22.7-0.2 is located above the GMC along the Galactic latitude direction (see also Figure 3).

cate that W41 lies on the redshifted side with respect to the systemic velocity of bubble, while G22.7-0.2 lies on the blueshifted side. From the spatial correspondence between the radio shells and the molecular clouds, W41 shows interaction with the molecular gas at the shell center, whereas G22.7-0.2 shows interaction along the shell rim (Figures 2, 3, and Section 4.1.2). These results suggest that the three-dimensional configuration places W41 in front of the GMC and G22.7-0.2 slightly behind or at nearly the same distance as the GMC.

Based on these considerations, we present in Figure 6, a schematic view of the line-of-sight locations of the two SNRs and the GMC. This schematic is consistent with the spatial and kinematic analyses described in this section. In any case, determining the true three-dimensional locations of the objects solely from radio continuum and line data remains extremely challenging. Future measurements of stellar three-dimensional motions in this region will provide critical clues for clarifying the positional relationship between the molecular clouds and the SNRs. Observations with Gaia and the upcoming infrared astrometric satellite JASMINE (e.g., Gouda 2012) are particularly promising in this regard.

#### 4.2. Total ISM Protons

From Section 4.1, the velocity ranges of the clouds associated with W41 and G22.7-0.2 have been identified. In this section, we estimate the total number of ISM protons in both molecular and atomic phases in order to compare with the gamma-ray emission. If the gamma rays are of hadronic origin, their spatial distribution should correspond to that of the target ISM. To this end, we first identify the clouds spatially associated

with the gamma-ray-emitting regions in each SNR (Section 4.2.1). We then estimate the molecular gas mass from the CO data (Section 4.2.2), followed by an evaluation of the atomic gas mass from the HI data (Section 4.2.3).

##### 4.2.1. Identification of Target Clouds

According to Figure 1(b), W41 shows a gamma-ray peak at the central region of its radio shell ( $l, b$ ) = (23°3, −0°3), while G22.7-0.2 exhibits a peak on the southern part of its shell ( $l, b$ ) = (22°5, −0°2). Thus, the ISM clouds corresponding to these locations are expected to serve as the target gas. On the other hand, because the HI spectra exhibit self-absorption due to cold HI (see Section 3.3), it is difficult to establish a direct spatial correlation with the gamma rays. Therefore, we used the  $^{12}\text{CO}(J = 1-0)$  data to identify the relevant clouds.

Analysis of the channel maps (Figures 2 and 3) shows that molecular clouds in the velocity range of +55–+80 km s<sup>−1</sup> for W41 and +76–+85 km s<sup>−1</sup> for G22.7-0.2 exhibit well spatial correspondence with the gamma-ray emission. Figure 7 presents the CO integrated intensity maps over these velocity intervals, overlaid with the gamma-ray significance contours. In both SNRs, strong CO emission is found to coincide with the gamma-ray peaks. We therefore identify these velocity ranges as the most plausible candidates for the ISM gas associated with the gamma-ray emission. It should be noted that the angular resolution of the gamma-ray data (~0°08) is lower than that of the CO and HI data; consequently, our comparison is limited to integrated spatial distributions rather than a direct point-to-point correspondence.

##### 4.2.2. Molecular Gas

The column density of molecular hydrogen,  $N(\text{H}_2)$ , was derived from the integrated intensity of the  $^{12}\text{CO}(J = 1-0)$  emission using the CO–H<sub>2</sub> conversion factor:

$$N(\text{H}_2) = X_{\text{CO}} W(\text{CO}) \text{ (cm}^{-2}\text{)}, \quad (1)$$

where  $X_{\text{CO}}$  is the CO–H<sub>2</sub> conversion factor and  $W(\text{CO})$  is the integrated intensity of the  $^{12}\text{CO}(J = 1-0)$  line. In this study, we adopted  $X_{\text{CO}} = 1.0 \times 10^{20} \text{ cm}^{-2} ((\text{K km s}^{-1})^{-1})$  (Okamoto et al. 2017). Using this method, the peak molecular column densities of the associated clouds in both SNRs were estimated to be  $\sim(1-2) \times 10^{22} \text{ cm}^{-2}$ . The proton column density of the molecular component is defined as  $N_p(\text{H}_2) = 2 \times N(\text{H}_2)$ .

The molecular cloud mass,  $M$ , was then calculated as

$$M = m_{\text{H}} \mu \Omega D^2 \sum_i N_i(\text{H}_2), \quad (2)$$

where  $m_{\text{H}}$  is the mass of a hydrogen atom,  $\mu = 2.8$  is the mean molecular weight per hydrogen molecule,  $\Omega$

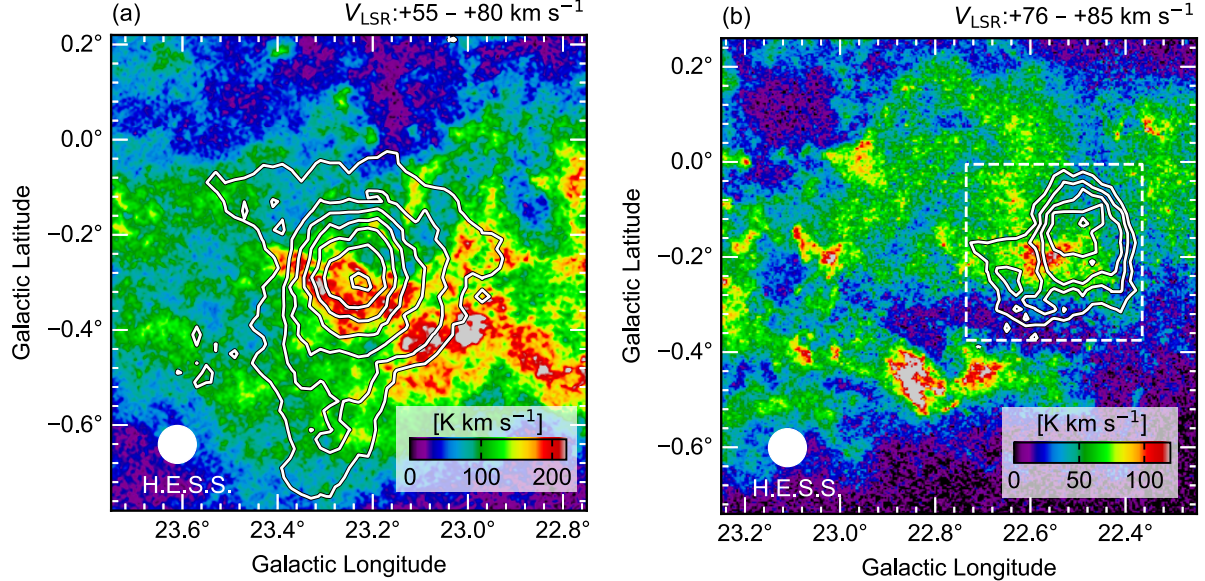


**Figure 7.** Integrated intensity maps of the  $^{12}\text{CO}(J = 1-0)$  emission toward (a) W41 at  $V_{\text{LSR}} = +55 - +80 \text{ km s}^{-1}$  and (b) G22.7–0.2 at  $V_{\text{LSR}} = +76 - +85 \text{ km s}^{-1}$ . The superposed contours are TeV gamma-ray significance maps. The contour levels are 5, 7, 9, 11, 13, and 15  $\sigma$  for (a) and 2, 3, 4, and 5  $\sigma$  for (b). The dashed rectangle in (b) shows the region of the TeV gamma-ray source HESS J1832–093. The PSF of H.E.S.S. is indicated by the gray circle shown in the lower left corner.

is the solid angle per pixel,  $D = 4.4$  kpc is the distance to the SNRs, and  $N_i(\text{H}_2)$  is the molecular column density at pixel  $i$ . The cloud size was defined as the half-maximum contour of the CO integrated intensity. Based on this procedure, we obtained molecular cloud masses of  $\sim 7.2 \times 10^4 M_{\odot}$  for W41 and  $\sim 2.4 \times 10^4 M_{\odot}$  for G22.7–0.2.

#### 4.2.3. Atomic Gas

In general, the atomic hydrogen column density is estimated under the assumption that the HI emission is optically thin. If this assumption holds, the column density of interstellar protons,  $N_p(\text{HI})$ , can be expressed as (Dickey & Lockman 1990):

$$N_p(\text{HI}) = 1.823 \times 10^{18} \int T_b(v), dV \text{ (cm}^{-2}\text{)}, \quad (3)$$

where  $T_b$  is the observed HI brightness temperature and  $v$  is the radial velocity. However, as discussed in Section 3.3, the HI spectra show absorption dips coincident with the CO velocity ranges, indicating that self-absorption by cold HI embedded in molecular clouds cannot be neglected. Therefore, corrections for optical depth effects must be considered. Indeed, (Fukui et al. 2012), based on an analysis of RX J1713.7–3946, showed that the optical depth of self-absorbing HI is typically  $\tau \sim 0.7$ , resulting in an increase of  $N_p(\text{HI})$  by a factor of  $\sim 1.2$  compared to the optically thin assumption.

The observed HI brightness temperature as a function of radial velocity,  $T_L(v)$ , can be expressed by the

radiative transfer equation (e.g., Sato & Fukui 1978):

$$T_L(v) = T_s \left[ 1 - e^{-\tau(v)} \right] + [T_L^{\text{BG}}(v) + T_C^{\text{BG}}] e^{-\tau(v)} - (T_C^{\text{FG}} + T_C^{\text{BG}}), \quad (4)$$

where  $T_L(v)$  is the observed HI brightness temperature,  $T_s$  is the spin temperature,  $\tau(v)$  is the optical depth of the cold HI cloud,  $T_L^{\text{FG}}(v)$  and  $T_L^{\text{BG}}(v)$  represent the foreground and background HI emission, and  $T_C^{\text{FG}}$  and  $T_C^{\text{BG}}$  denote the brightness temperatures of the foreground and background radio continuum emission, respectively. The background HI component,  $T_L^{\text{BG}}(v)$ , was estimated using the method described by Sato & Fukui (1978), in which a linear interpolation across the HI dip is applied (see the dashed line at position B in Figure 5). This approach generally provides a lower limit to the true absorption. Even when a parabolic interpolation is adopted instead of a linear one, the difference in the resulting correction remains within  $\sim 30\%$  (Sato & Fukui 1978). In the present study, we adopt the linear interpolation. Furthermore, based on the radio continuum emission measured from Figure 1(a), we assume  $T_C^{\text{FG}} = 0$  when estimating the optical depth.

We estimated the column density of cold HI,  $N_p(\text{HI})$ , toward position B in Figure 5, where the spatial correspondence between the gamma-ray emission and molecular clouds is strong and a clear HI dip is observed. Distinct HI dips are seen at  $+60 \text{ km s}^{-1}$  and  $+80 \text{ km s}^{-1}$ . The column density of cold HI, taking into account op-

tical depth effects, can be derived as

$$N_p(\mathrm{HI}) = 1.823 \times 10^{18} \int T_s \tau(v) dV \ (\mathrm{cm}^{-2}), \quad (5)$$

where  $T_s$  denotes the spin temperature. Direct measurements of the spin temperature of cold HI are generally difficult; however, for cold HI embedded in molecular clouds,  $T_s$  is expected to be comparable to the kinematic temperature of the molecular gas. This is because the typical density of molecular clouds ( $\sim 10^3 \mathrm{cm}^{-3}$ ) is high enough for collisions with  $\mathrm{H}_2$  molecules to thermalize the HI with the molecular gas. Since the critical density for collisional excitation of the  $^{12}\mathrm{CO}(J=1-0)$  transition is also  $\sim 10^3 \mathrm{cm}^{-3}$ , this assumption is reasonable in regions where CO emission is detected. From the depth of the HI dips at position B, we estimate  $T_s \sim 20 \mathrm{K}$  for the  $+60 \mathrm{km} \mathrm{s}^{-1}$  component and  $\lesssim 50 \mathrm{K}$  for the  $+80 \mathrm{km} \mathrm{s}^{-1}$  component. The CO peak temperature suggests a molecular gas temperature of  $\sim 15 \mathrm{K}$ . Based on these considerations, we calculated  $N_p(\mathrm{HI})$  for  $T_s = 20, 30$ , and  $40 \mathrm{K}$  within the velocity range of  $+55$ – $+80 \mathrm{km} \mathrm{s}^{-1}$  (as defined in Section 4.2.1). The resulting HI column densities are  $(4.5\text{--}5.5) \times 10^{21} \mathrm{cm}^{-2}$ , with maximum optical depths of  $\tau \sim 0.8\text{--}1.1$ . These values are approximately a factor of 2.5 higher than those derived under the optically thin assumption. At position B, the molecular proton column density is  $N_p(\mathrm{H}_2) \sim 3.7 \times 10^{22} \mathrm{cm}^{-2}$ ; therefore, even after correcting for self-absorption, the contribution of HI remains limited to 12–15% of the total proton column density. Applying the same method to position F (toward G22.7–0.2), we obtained  $N_p(\mathrm{HI}) \sim (0.8\text{--}1.0) \times 10^{21} \mathrm{cm}^{-2}$  with maximum optical depths of  $\tau \sim 0.4\text{--}0.5$ , corresponding to only 6–8% of the total proton column density. These results indicate that the bulk of the interstellar protons associated with the gamma-ray emission originates from molecular hydrogen rather than atomic hydrogen.

From the above analysis, we conclude that the dominant component of the target protons for the gamma-ray emission in both W41 and G22.7–0.2 is molecular hydrogen. Finally, using the molecular cloud masses derived in Section 4.2.2, we estimated the mean proton number density. The cloud volume was calculated from the equivalent radius based on the projected area of each molecular cloud. As a result, we obtained  $n_p \sim 1.2 \times 10^3 \mathrm{cm}^{-3}$  for W41 and  $n_p \sim 5.3 \times 10^2 \mathrm{cm}^{-3}$  for G22.7–0.2.

#### 4.3. Total Energy of CR Protons

In this section, we estimate the total energy of accelerated cosmic-ray protons ( $W_p$ ) in both SNRs and discuss the relation between SNR age and  $W_p$ . Previous studies have reported that for young SNRs with ages  $\lesssim 6 \mathrm{kyr}$ ,  $W_p$  tends to increase with age, while for middle-aged SNRs with ages  $\gtrsim 8 \mathrm{kyr}$ ,  $W_p$  decreases (e.g., Sano et al. 2021a,b; Aruga et al. 2022). If this observational trend holds, both W41 and G22.7–0.2, which are classified as

middle-aged SNRs, are expected to exhibit lower  $W_p$  values compared to the peak. In this study, we focus in particular on the diffusion of cosmic rays in middle-aged SNRs.

The total energy of accelerated CR protons,  $W_p$ , can be derived under the assumption that the hadronic process dominates, as follows (e.g., Aharonian et al. 2006):

$$W_p \sim t_{pp \rightarrow \pi^0} L_\gamma \ (\mathrm{erg}), \quad (6)$$

where  $t_{pp \rightarrow \pi^0} \sim 4.5 \times 10^{13} \left(\frac{n_p}{100 \mathrm{cm}^{-3}}\right)^{-1} \mathrm{s}$  is the cooling time of CR protons through inelastic p–p interactions, and  $L_\gamma$  is the gamma-ray luminosity in units of  $\mathrm{erg} \mathrm{s}^{-1}$ . From Suzuki et al. (2022), based on GeV and TeV spectra obtained from Fermi-LAT and H.E.S.S., the gamma-ray luminosity associated with W41 is estimated to be  $L_\gamma \sim 8.27(7.74\text{--}8.89) \times 10^{34} \mathrm{erg} \mathrm{s}^{-1}$ . Using  $n_p \sim 1.2 \times 10^3 \mathrm{cm}^{-3}$ , we obtain  $W_p \sim (3.2 \pm 0.2) \times 10^{47} \mathrm{erg}$ . In the case of G22.7–0.2, the gamma-ray luminosity is estimated to be  $L_\gamma \sim 1.36(1.23\text{--}1.51) \times 10^{35} \mathrm{erg} \mathrm{s}^{-1}$ , based on pion-decay model fitting to the combined Fermi and H.E.S.S. spectra assuming a spectral index of 2.6 (H.E.S.S. Collaboration et al. 2015). Adopting  $n_p \sim 5.3 \times 10^2 \mathrm{cm}^{-3}$  yields  $W_p \sim (1.2 \pm 0.1) \times 10^{48} \mathrm{erg}$ . The  $W_p$  values obtained in this study correspond to only 0.03–0.1% of the typical kinematic energy released by a supernova explosion ( $\sim 10^{51} \mathrm{erg}$ ).

Figure 8 shows SNR age– $W_p$  relation for 15 gamma-ray SNRs, including W41 and G22.7–0.2. Both remnants show values consistent with other middle-aged SNRs such as Puppis A (Aruga et al. 2022), and G346.6–0.2 (Sano et al. 2021a). Our results support the interpretation that a large fraction of CR protons escape from the SNR shell on timescales of  $\sim 10^4 \mathrm{yr}$ , leading to the reduced  $W_p$  observed at present. This scenario is also supported by estimates of the CR diffusion length (see also Aruga et al. 2022). An important point is that the  $W_p$  of W41 is comparable to that of SN 1006, the youngest SNR ( $\sim 1.0 \mathrm{kyr}$ ) in the previously age– $W_p$  plot. This provides an important constraint on the timescale of acceleration and escape of CRs over  $\sim 1\text{--}60 \mathrm{kyr}$ . It should be noted, however, that  $W_p$  for most SNRs is derived solely from spectral energy distribution modeling. This method has inherent uncertainties by a factor of 2–3 due to the difficulty in disentangling hadronic from leptonic gamma-ray components (Inoue et al. 2012). In addition, the estimate of  $n_p$  involves uncertainties associated with the CO-to- $\mathrm{H}_2$  conversion factor, typically at the level of  $\sim 30\%$ . Nevertheless, these uncertainties do not alter the overall trend observed in the age– $W_p$  relation.

## 5. CONCLUSIONS

In this study, we investigated the interaction between interstellar gas and two middle-aged gamma-ray SNRs, W41 and G22.7–0.2, using high-resolution CO and HI data obtained with the Nobeyama 45-m telescope and the VLA. We identified the velocity ranges

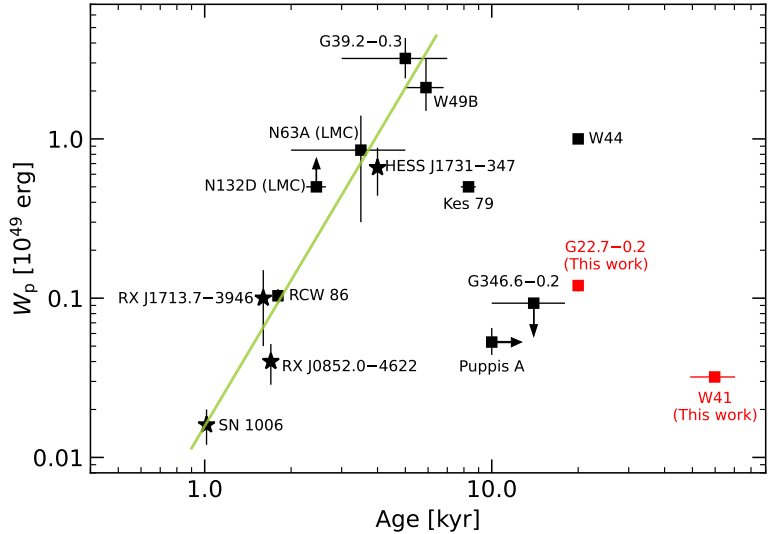


**Figure 8.** Scatter plot between the SNR age and the total energy of the cosmic-ray protons  $W_p$  (e.g., Sano et al. 2021a,b, 2022; Aruga et al. 2022). The green line indicates the linear regression of the double-logarithmic plot applying least-squares fitting to the data points with the ages of SNRs below 6 kyr. The plots of SN 1006, RX J0852.0-4622, RX J1713.7-3946 and HESS J1731-347 consider the contribution of hadronic gamma-rays to the total gamma-rays (Fukuda et al. 2014; Fukui et al. 2021, 2024; Sano et al. 2022).

of molecular and atomic clouds physically associated with the two SNRs as  $+50 \pm 80$  km s $^{-1}$  for W41 and  $+76 \pm 110$  km s $^{-1}$  for G22.7-0.2. These clouds show good spatial correspondence with the radio shells, and in the case of W41, also with shock-excited OH masers. The cavity-like structures observed in the  $l$ - $v$  diagrams are interpreted as low-density bubbles created by stellar winds that are now interacting with the subsequent supernova shocks.

From column density analyses of the molecular and atomic gas, we found that molecular hydrogen dominates the total ISM proton content associated with both SNRs. The contribution from atomic hydrogen is less than 10%, and this remains the case even after correcting for self-absorption. The average proton densities were estimated to be  $\sim 1.2 \times 10^3$  cm $^{-3}$  for W41 and  $\sim 5.3 \times 10^2$  cm $^{-3}$  for G22.7-0.2.

By comparing with the gamma-ray luminosities, we estimated the total energy of accelerated CR protons to be  $W_p \sim 3.2 \times 10^{47}$  erg for W41 and  $\sim 1.2 \times 10^{48}$  erg for G22.7-0.2. These values correspond to only 0.03–0.1% of the canonical kinematic energy of a supernova explosion ( $\sim 10^{51}$  erg). Additionally, these values are consistent with the reported age– $W_p$  relation in previous studies. In particular, the  $W_p$  of W41 is comparable to that of SN 1006, a younger SNR ( $\sim 1.0$  kyr), providing important constraints on the evolutionary timescale of CR proton acceleration and escape.

Future prospects include studying the interaction of escaped CRs with surrounding molecular clouds, which can produce secondary hadronic gamma-ray emission. Recent gamma-ray observations have reported a num-

ber of unidentified sources (e.g., Aharonian et al. 2008a; Abeysekara et al. 2017), some of which may be explained by such secondary emission from escaped CRs. Indeed, observational evidence for this scenario has already been suggested in SNRs such as W28 and W44 (e.g., Aharonian et al. 2008b; Uchiyama et al. 2012). For W41 and G22.7-0.2, molecular clouds other than those identified in this study could also serve as potential targets for escaped CRs. Future high-sensitivity gamma-ray observations with CTA will be crucial for detecting such secondary hadronic gamma-ray emission. Exploring the interaction between escaped CRs and the ISM will provide valuable constraints on the spatial and energy dependence of CR diffusion, thereby advancing our understanding of the underlying diffusion mechanisms.

We are grateful to the anonymous referee for carefully reading our manuscript and giving us thoughtful suggestions, which improved our paper. The 45-m radio telescope is operated by the Nobeyama Radio Observatory, a branch of the National Astronomical Observatory of Japan (NAOJ). This publication makes use of data from FUGIN, FOREST Unbiased Galactic plane Imaging survey with the Nobeyama 45-m telescope, a legacy project in the Nobeyama 45-m radio telescope. The scientific results reported in this article are based on data obtained from the H.E.S.S. Data Archive. We express our sincere gratitude to all the staff who contributed to the construction and operation of H.E.S.S. We thank Mr. Zachary Smeaton for his helpful discussions and valuable comments on the manuscript. This work was supported by a University Research Support Grant from NAOJ. It was also supported by JSPS KAKENHI Grant Numbers JP24H00246 (HS). This work was also supported by CCI Holdings Co., Ltd. This manuscript was compiled using Overleaf, a very useful free online LaTeX editor.

*Facilities:* Nobeyama 45-m radio telescope (NRO45), The Very Large Array (VLA), High Energy Stereoscopic System (H.E.S.S.).

*Software:* astropy (Astropy Collaboration et al. 2013, 2018), aplpy (Robitaille & Bressert 2012; Robitaille 2019), matplotlib (Hunter 2007), numpy (Harris et al. 2020), Scipy (Virtanen et al. 2020).

## REFERENCES

Abeysekara, A. U., Albert, A., Alfaro, R., et al. 2017, *Science*, 358, 911, doi: [10.1126/science.aan4880](https://doi.org/10.1126/science.aan4880)

Aharonian, F., Akhperjanian, A. G., Bazer-Bachi, A. R., et al. 2006, *A&A*, 449, 223, doi: [10.1051/0004-6361:20054279](https://doi.org/10.1051/0004-6361:20054279)

Aharonian, F., Akhperjanian, A. G., Barres de Almeida, U., et al. 2008a, *A&A*, 477, 353, doi: [10.1051/0004-6361:20078516](https://doi.org/10.1051/0004-6361:20078516)

Aharonian, F., Akhperjanian, A. G., Bazer-Bachi, A. R., et al. 2008b, *A&A*, 481, 401, doi: [10.1051/0004-6361:20077765](https://doi.org/10.1051/0004-6361:20077765)

Aharonian, F. A., & Atoyan, A. M. 1996, *A&A*, 309, 917

Albert, J., Aliu, E., Anderhub, H., et al. 2006, *ApJL*, 643, L53, doi: [10.1086/504917](https://doi.org/10.1086/504917)

Allen, M., & Robinson, G. W. 1977, *ApJ*, 212, 396, doi: [10.1086/155059](https://doi.org/10.1086/155059)

Arikawa, Y., Tatematsu, K., Sekimoto, Y., & Takahashi, T. 1999, *PASJ*, 51, L7, doi: [10.1093/pasj/51.4.L7](https://doi.org/10.1093/pasj/51.4.L7)

Aruga, M., Sano, H., Fukui, Y., et al. 2022, *ApJ*, 938, 94, doi: [10.3847/1538-4357/ac90c6](https://doi.org/10.3847/1538-4357/ac90c6)

Astropy Collaboration, Robitaille, T. P., Tollerud, E. J., et al. 2013, *A&A*, 558, A33, doi: [10.1051/0004-6361/201322068](https://doi.org/10.1051/0004-6361/201322068)

Astropy Collaboration, Price-Whelan, A. M., Sipőcz, B. M., et al. 2018, *AJ*, 156, 123, doi: [10.3847/1538-3881/aabc4f](https://doi.org/10.3847/1538-3881/aabc4f)

Bell, A. R. 1978, *MNRAS*, 182, 147, doi: [10.1093/mnras/182.2.147](https://doi.org/10.1093/mnras/182.2.147)

Blandford, R. D., & Ostriker, J. P. 1978, *ApJL*, 221, L29, doi: [10.1086/182658](https://doi.org/10.1086/182658)

Broersen, S., Chiotellis, A., Vink, J., & Bamba, A. 2014, *MNRAS*, 441, 3040, doi: [10.1093/mnras/stu667](https://doi.org/10.1093/mnras/stu667)

Brunthaler, A., Reid, M. J., Menten, K. M., et al. 2009, *ApJ*, 693, 424, doi: [10.1088/0004-637X/693/1/424](https://doi.org/10.1088/0004-637X/693/1/424)

Castro, D., Slane, P., Carlton, A., & Figueroa-Feliciano, E. 2013, *ApJ*, 774, 36, doi: [10.1088/0004-637X/774/1/36](https://doi.org/10.1088/0004-637X/774/1/36)

Chibueze, J. O., Ugwu, C. J., Hirota, T., et al. 2025, *MNRAS*, 539, 145, doi: [10.1093/mnras/stae2773](https://doi.org/10.1093/mnras/stae2773)

Dickey, J. M., & Lockman, F. J. 1990, *ARA&A*, 28, 215, doi: [10.1146/annurev.aa.28.090190.001243](https://doi.org/10.1146/annurev.aa.28.090190.001243)

Drury, L. O. 1983, *Reports on Progress in Physics*, 46, 973, doi: [10.1088/0034-4885/46/8/002](https://doi.org/10.1088/0034-4885/46/8/002)

Dwarkadas, V. V. 2005, *ApJ*, 630, 892, doi: [10.1086/432109](https://doi.org/10.1086/432109)

Ellison, D. C., Patnaude, D. J., Slane, P., & Raymond, J. 2010, *ApJ*, 712, 287, doi: [10.1088/0004-637X/712/1/287](https://doi.org/10.1088/0004-637X/712/1/287)

Emerson, D. T., & Graeve, R. 1988, *A&A*, 190, 353

Frail, D. A., Claussen, M. J., & Méhault, J. 2013, *ApJL*, 773, L19, doi: [10.1088/2041-8205/773/2/L19](https://doi.org/10.1088/2041-8205/773/2/L19)

Fujisawa, K., Sugiyama, K., Motogi, K., et al. 2014, *PASJ*, 66, 31, doi: [10.1093/pasj/psu015](https://doi.org/10.1093/pasj/psu015)

Fukuda, T., Yoshiike, S., Sano, H., et al. 2014, *The Astrophysical Journal*, 788, 94, doi: [10.1088/0004-637X/788/1/94](https://doi.org/10.1088/0004-637X/788/1/94)

Fukui, Y., Aruga, M., Sano, H., et al. 2024, *ApJ*, 961, 162, doi: [10.3847/1538-4357/ad0da3](https://doi.org/10.3847/1538-4357/ad0da3)

Fukui, Y., Mizuno, N., & Onishi, T. 2003, in IAU Symposium, Vol. 221, IAU Symposium, P224

Fukui, Y., Sano, H., Yamane, Y., et al. 2021, *ApJ*, 915, 84, doi: [10.3847/1538-4357/abff4a](https://doi.org/10.3847/1538-4357/abff4a)

Fukui, Y., Torii, K., Onishi, T., et al. 2015, *ApJ*, 798, 6, doi: [10.1088/0004-637X/798/1/6](https://doi.org/10.1088/0004-637X/798/1/6)

Fukui, Y., Sano, H., Sato, J., et al. 2012, *ApJ*, 746, 82, doi: [10.1088/0004-637X/746/1/82](https://doi.org/10.1088/0004-637X/746/1/82)

—. 2017, *ApJ*, 850, 71, doi: [10.3847/1538-4357/aa9219](https://doi.org/10.3847/1538-4357/aa9219)

Fukushima, K., Yamaguchi, H., Slane, P. O., et al. 2020, *ApJ*, 897, 62, doi: [10.3847/1538-4357/ab94a6](https://doi.org/10.3847/1538-4357/ab94a6)

Gabici, S. 2013, in *Astrophysics and Space Science Proceedings*, Vol. 34, *Cosmic Rays in Star-Forming Environments*, ed. D. F. Torres & O. Reimer, 221, doi: [10.1007/978-3-642-35410-6\\_16](https://doi.org/10.1007/978-3-642-35410-6_16)

Gouda, N. 2012, in *Astronomical Society of the Pacific Conference Series*, Vol. 458, *Galactic Archaeology: Near-Field Cosmology and the Formation of the Milky Way*, ed. W. Aoki, M. Ishigaki, T. Suda, T. Tsujimoto, & N. Arimoto, 417

H. E. S. S. Collaboration, Abramowski, A., Acero, F., et al. 2015, *MNRAS*, 446, 1163, doi: [10.1093/mnras/stu2148](https://doi.org/10.1093/mnras/stu2148)

H. E. S. S. Collaboration, Abdalla, H., Abramowski, A., et al. 2018, *A&A*, 612, A1, doi: [10.1051/0004-6361/201732098](https://doi.org/10.1051/0004-6361/201732098)

Harris, C. R., Millman, K. J., van der Walt, S. J., et al. 2020, *Nature*, 585, 357, doi: [10.1038/s41586-020-2649-2](https://doi.org/10.1038/s41586-020-2649-2)

Helfand, D. J., Becker, R. H., White, R. L., Fallon, A., & Tuttle, S. 2006, *AJ*, 131, 2525, doi: [10.1086/503253](https://doi.org/10.1086/503253)

Hess, V. 1912, *Phys.Z.*, 13, 1084

Hogge, T. G., Jackson, J. M., Allingham, D., et al. 2019, *ApJ*, 887, 79, doi: [10.3847/1538-4357/ab5180](https://doi.org/10.3847/1538-4357/ab5180)

Hunter, J. D. 2007, *Computing in Science & Engineering*, 9, 90, doi: [10.1109/MCSE.2007.55](https://doi.org/10.1109/MCSE.2007.55)

Inoue, T., Yamazaki, R., & Inutsuka, S.-i. 2009, *ApJ*, 695, 825, doi: [10.1088/0004-637X/695/2/825](https://doi.org/10.1088/0004-637X/695/2/825)

Inoue, T., Yamazaki, R., Inutsuka, S.-i., & Fukui, Y. 2012, *ApJ*, 744, 71, doi: [10.1088/0004-637X/744/1/71](https://doi.org/10.1088/0004-637X/744/1/71)

Ito, D., Sano, H., Nakazawa, K., et al. 2025, *ApJ*, 978, 123, doi: [10.3847/1538-4357/ad95f5](https://doi.org/10.3847/1538-4357/ad95f5)

Koo, B.-C., & Heiles, C. 1991, *ApJ*, 382, 204, doi: [10.1086/170709](https://doi.org/10.1086/170709)

Koo, B.-C., & McKee, C. F. 1992, *ApJ*, 388, 93, doi: [10.1086/171132](https://doi.org/10.1086/171132)

Koo, B.-C., Reach, W. T., Heiles, C., Fesen, R. A., & Shull, J. M. 1990, *ApJ*, 364, 178, doi: [10.1086/169400](https://doi.org/10.1086/169400)

Kuno, N., Takano, S., Iono, D., et al. 2011, in *2011 XXXth URSI General Assembly and Scientific Symposium*, 1–4, doi: [10.1109/URSIGASS.2011.6051296](https://doi.org/10.1109/URSIGASS.2011.6051296)

Kuriki, M., Sano, H., Kuno, N., et al. 2018, *ApJ*, 864, 161, doi: [10.3847/1538-4357/aad7be](https://doi.org/10.3847/1538-4357/aad7be)

Landecker, T. L., Pineault, S., Routledge, D., & Vaneldik, J. F. 1989, *MNRAS*, 237, 277, doi: [10.1093/mnras/237.1.277](https://doi.org/10.1093/mnras/237.1.277)

Leahy, D. A., & Tian, W. W. 2008, *AJ*, 135, 167, doi: [10.1088/0004-6256/135/1/167](https://doi.org/10.1088/0004-6256/135/1/167)

Lee, S.-H., Slane, P. O., Ellison, D. C., Nagataki, S., & Patnaude, D. J. 2013, *ApJ*, 767, 20, doi: [10.1088/0004-637X/767/1/20](https://doi.org/10.1088/0004-637X/767/1/20)

Messineo, M., Figer, D. F., Davies, B., et al. 2010, *ApJ*, 708, 1241, doi: [10.1088/0004-637X/708/2/1241](https://doi.org/10.1088/0004-637X/708/2/1241)

Messineo, M., Menten, K. M., Figer, D. F., et al. 2014, *A&A*, 569, A20, doi: [10.1051/0004-6361/201322822](https://doi.org/10.1051/0004-6361/201322822)

Minamidani, T., Nishimura, A., Miyamoto, Y., et al. 2016, in *Millimeter, Submillimeter, and Far-Infrared Detectors and Instrumentation for Astronomy VIII*, Vol. 9914, 99141Z, doi: [10.1117/12.2232137](https://doi.org/10.1117/12.2232137)

Müller, P., Krause, M., Beck, R., & Schmidt, P. 2017, *A&A*, 606, A41, doi: [10.1051/0004-6361/201731257](https://doi.org/10.1051/0004-6361/201731257)

Ohira, Y., Murase, K., & Yamazaki, R. 2010, *A&A*, 513, A17, doi: [10.1051/0004-6361/200913495](https://doi.org/10.1051/0004-6361/200913495)

Okamoto, R., Yamamoto, H., Tachihara, K., et al. 2017, *ApJ*, 838, 132, doi: [10.3847/1538-4357/aa6747](https://doi.org/10.3847/1538-4357/aa6747)

Robitaille, T. 2019, *APLpy v2.0: The Astronomical Plotting Library in Python*, doi: [10.5281/zenodo.2567476](https://doi.org/10.5281/zenodo.2567476)

Robitaille, T., & Bressert, E. 2012, *APLpy: Astronomical Plotting Library in Python*. <http://ascl.net/1208.017>

Sano, H., Suzuki, H., Nobukawa, K. K., et al. 2021a, *ApJ*, 923, 15, doi: [10.3847/1538-4357/ac1c02](https://doi.org/10.3847/1538-4357/ac1c02)

Sano, H., Yamaguchi, H., Aruga, M., et al. 2022, *ApJ*, 933, 157, doi: [10.3847/1538-4357/ac7465](https://doi.org/10.3847/1538-4357/ac7465)

Sano, H., Tanaka, T., Torii, K., et al. 2013, *ApJ*, 778, 59, doi: [10.1088/0004-637X/778/1/59](https://doi.org/10.1088/0004-637X/778/1/59)

Sano, H., Yamane, Y., Voisin, F., et al. 2017, *ApJ*, 843, 61, doi: [10.3847/1538-4357/aa73e0](https://doi.org/10.3847/1538-4357/aa73e0)

Sano, H., Yamane, Y., Tokuda, K., et al. 2018, *ApJ*, 867, 7, doi: [10.3847/1538-4357/aae07c](https://doi.org/10.3847/1538-4357/aae07c)

Sano, H., Matsumura, H., Yamane, Y., et al. 2019, *ApJ*, 881, 85, doi: [10.3847/1538-4357/ab2ade](https://doi.org/10.3847/1538-4357/ab2ade)

Sano, H., Yoshiike, S., Yamane, Y., et al. 2021b, *ApJ*, 919, 123, doi: [10.3847/1538-4357/ac0dba](https://doi.org/10.3847/1538-4357/ac0dba)

Sano, H., Yamane, Y., van Loon, J. T., et al. 2023, *ApJ*, 958, 53, doi: [10.3847/1538-4357/acffbe](https://doi.org/10.3847/1538-4357/acffbe)

Sato, F., & Fukui, Y. 1978, *AJ*, 83, 1607, doi: [10.1086/112370](https://doi.org/10.1086/112370)

Sawada, T., Ikeda, N., Sunada, K., et al. 2008, *PASJ*, 60, 445, doi: [10.1093/pasj/60.3.445](https://doi.org/10.1093/pasj/60.3.445)

Sofue, Y. 2019, *PASJ*, 71, 121, doi: [10.1093/pasj/psz106](https://doi.org/10.1093/pasj/psz106)

Sofue, Y., & Reich, W. 1979, *A&AS*, 38, 251

Stafford, J. N., Lopez, L. A., Auchettl, K., & Holland-Ashford, T. 2019, ApJ, 884, 113, doi: [10.3847/1538-4357/ab3a33](https://doi.org/10.3847/1538-4357/ab3a33)

Stil, J. M., Taylor, A. R., Dickey, J. M., et al. 2006, AJ, 132, 1158, doi: [10.1086/505940](https://doi.org/10.1086/505940)

Su, Y., Yang, J., Zhou, X., Zhou, P., & Chen, Y. 2014, ApJ, 796, 122, doi: [10.1088/0004-637X/796/2/122](https://doi.org/10.1088/0004-637X/796/2/122)

Su, Y., Zhang, S., Shao, X., & Yang, J. 2015, ApJ, 811, 134, doi: [10.1088/0004-637X/811/2/134](https://doi.org/10.1088/0004-637X/811/2/134)

Suzuki, H., Bamba, A., & Shibata, S. 2021, ApJ, 914, 103, doi: [10.3847/1538-4357/abfb02](https://doi.org/10.3847/1538-4357/abfb02)

Suzuki, H., Bamba, A., Yamazaki, R., & Ohira, Y. 2022, ApJ, 924, 45, doi: [10.3847/1538-4357/ac33b5](https://doi.org/10.3847/1538-4357/ac33b5)

Tam, P.-H. T., Lee, K. K., Cui, Y., et al. 2020, ApJ, 899, 75, doi: [10.3847/1538-4357/ab9e76](https://doi.org/10.3847/1538-4357/ab9e76)

Telezhinsky, I., Dwarkadas, V. V., & Pohl, M. 2012, Astroparticle Physics, 35, 300, doi: [10.1016/j.astropartphys.2011.10.001](https://doi.org/10.1016/j.astropartphys.2011.10.001)

Thompson, M. A., Hatchell, J., Walsh, A. J., MacDonald, G. H., & Millar, T. J. 2006, A&A, 453, 1003, doi: [10.1051/0004-6361:20054383](https://doi.org/10.1051/0004-6361:20054383)

Tsuji, N., Uchiyama, Y., Khangulyan, D., & Aharonian, F. 2021, ApJ, 907, 117, doi: [10.3847/1538-4357/abce65](https://doi.org/10.3847/1538-4357/abce65)

Uchiyama, Y., Funk, S., Katagiri, H., et al. 2012, ApJL, 749, L35, doi: [10.1088/2041-8205/749/2/L35](https://doi.org/10.1088/2041-8205/749/2/L35)

Umemoto, T., Minamidani, T., Kuno, N., et al. 2017, PASJ, 69, 78, doi: [10.1093/pasj/psx061](https://doi.org/10.1093/pasj/psx061)

Virtanen, P., Gommers, R., Oliphant, T. E., et al. 2020, Nature Methods, 17, 261, doi: [10.1038/s41592-019-0686-2](https://doi.org/10.1038/s41592-019-0686-2)

Weaver, R., McCray, R., Castor, J., Shapiro, P., & Moore, R. 1977, ApJ, 218, 377, doi: [10.1086/155692](https://doi.org/10.1086/155692)

Yang, R.-z., Zhang, X., Yuan, Q., & Liu, S. 2014, A&A, 567, A23, doi: [10.1051/0004-6361/201322737](https://doi.org/10.1051/0004-6361/201322737)

Yeung, P. K. H., Bamba, A., & Sano, H. 2023, PASJ, 75, 384, doi: [10.1093/pasj/psad006](https://doi.org/10.1093/pasj/psad006)

Yoshiike, S., Fukuda, T., Sano, H., et al. 2013, ApJ, 768, 179, doi: [10.1088/0004-637X/768/2/179](https://doi.org/10.1088/0004-637X/768/2/179)